
Nonlinear motion separation via untrained generator networks with disentangled latent space variables and applications to cardiac MRI

Abdullah

Department of Mathematics
The Chinese University of Hong Kong, Hong Kong
abdullahuom1@yahoo.co

Martin Holler

Institute of Mathematics and Scientific Computing
University of Graz, Austria
martin.holler@uni-graz.at

Karl Kunisch

Institute of Mathematics and Scientific Computing
University of Graz, Austria
karl.kunisch@uni-graz.at

Malena Sabate Landman

Department of Applied Mathematics and Theoretical Physics
University of Cambridge, UK
ms2845@cam.ac.uk

Abstract

In this paper, a nonlinear approach to separate different motion types in video data is proposed. This is particularly relevant in dynamic medical imaging (e.g. PET, MRI), where patient motion poses a significant challenge due to its effects on the image reconstruction as well as for its subsequent interpretation. Here, a new method is proposed where dynamic images are represented as the forward mapping of a sequence of latent variables via a generator neural network. The latent variables are structured so that temporal variations in the data are represented via dynamic latent variables, which are independent of static latent variables characterizing the general structure of the frames. In particular, different kinds of motion are also characterized independently of each other via latent space disentanglement using one-dimensional prior information on all but one of the motion types. This representation allows to freeze any selection of motion types, and to obtain accurate independent representations of other dynamics of interest. Moreover, the proposed algorithm is training-free, i.e., all the network parameters are learned directly from a single video. We illustrate the performance of this method on phantom and real-data MRI examples, where we successfully separate respiratory and cardiac motion.

1 Introduction

One of the big challenges in dynamic imaging is to efficiently isolate the dynamics of interest from an array of intentional and unintentional motions, e.g. respiratory motion, contrast dynamics, cardiac motion and external motion. This is relevant in many imaging modalities such as positron emission tomography (PET) or computed tomography (CT), and particularly challenging in magnetic resonance imaging (MRI) and multimodality imaging that combines PET-CT and PET-MRI, since undesired motion can cause under and over-estimation of kinetic parameters, misinterpretation, blurring, ghosting, and unwanted signal enhancement artifacts [1, 2, 3, 4, 5, 6]. To overcome this problem, motion estimation has been a subject of significant research interest in a range of imaging modalities [8, 9, 10, 11, 12]. Several computational techniques for acquisitions and correction of motion and motion-corrected image reconstruction have been developed in parallel to the advancement of hardware [13, 14, 15, 16, 17, 18, 19]. Image-based motion synchronization and detection has been studied in [20, 21, 22], where filtering is used to separate respiratory and cardiac signals in PET.

In this paper we consider examples in dynamic MRI, where both deliberate imaging dynamics such as morphological motion or contrast inflow as well as undesired dynamics such as breathing motion play an important role. The latter are particularly challenging due to long acquisition times in MRI, which is especially relevant when long breath holds during image acquisition are not possible, e.g. with young children or patients with health problems. In these cases, there is a need for computational techniques to eliminate the respiratory motion from the final reconstruction. Traditionally, research has focused on motion correction, which consists in eliminating undesirable dynamics from the videos. In particular, image reconstruction for MRI with motion correction has been studied in detail, see [14, 23, 24] and the references therein. Most motion compensation strategies have not found widespread acceptance in clinical practice, mainly due to the complexity of their implementation and the associated cost or computational burden [13, 14]. In this work we develop a method based on generator neural networks that exhibits very successful results in motion separation for cardiac MRI images with respiratory motion.

1.1 Deep learning-based image and video reconstruction

Deep convolutional networks have been demonstrated to be powerful tools for image generation and provide excellent results when solving inverse problems involving image reconstruction [25, 26, 27, 29, 30, 31]. In particular, both supervised and unsupervised deep-learning-based algorithms were used in dynamic MRI to obtain fast and accurate reconstructions [32, 33, 34, 35]. However, network training usually comes at a huge computational cost and requires a large amount of training data; moreover, it is susceptible to bias originated in either the training datasets or in the training process through mode collapse. To overcome these shortcomings, the deep image prior (DIP) framework [25] presents a purely unsupervised method with neither pre-training nor external training data, where the structure of a generative network has the role of an image prior and shows excellent results in a variety of standard inverse problems such as super-resolution, denoising and inpainting. This is very relevant in the medical imaging context, where the data is very high dimensional. In fact, the DIP framework was applied to PET-MRI image reconstruction [36]. Moreover, the joint optimization of latent codes and network parameters was used for video compression [37], and a generalized time-dependent deep image prior was developed to generate dynamic MR images [38].

The use of generative adversarial networks (GANs) for video applications is a very extended topic of research; the most well known GANs being VGAN [39], TGAN [40] and MoCoGAN [41]. Unsupervised latent space disentanglement was proposed for infoGANs [42]. There, the input noise vector of the generative network is divided in two parts: z , which is treated as the source of incompressible noise, and c , which targets the salient structured semantic features of the data distribution and is called latent code. The idea of disentangling the latent space was also used for unsupervised semantic face editing in [43]. Latent space optimization maps one learnable noise vector to the image by minimizing a simple reconstruction loss. The idea of optimizing over the latent space of a generative network was studied in detail in [44].

1.2 Contribution of the paper

This paper proposes a new method for motion separation which, contrary to traditional motion correction, allows full independent reconstructions of the different dynamics present in the data.

This strategy is based on the optimization of an untrained generator network, where latent space disentanglement is achieved by imposing suitable conditions and assuming that one-dimensional information on all but one of the movements is known. To the best of our knowledge, this is the first time that latent space disentanglement is used in combination with untrained generators.

The method has some strong advantages with respect to trained generative models. Namely, it does not require big datasets which might be difficult to obtain, store and process; in fact, it just assumes that a single video is available. This reduces the computational cost drastically. It also provides robustness to potential bias in the data. Moreover, generating different motions independently allows for the reconstruction of unseen combination of motion states and for out-of-domain motion estimation. Moreover, the method requires one-dimensional information about one type of movement, but it does not assume physical knowledge on the observed dynamics. This is a reasonable assumption in practice, since one-dimensional information can be easily measured, e.g., via electrocardiograms or accelerometer data. The performance of the method is evaluated by numerical examples for dynamic MRI presenting respiratory and cardiac motions.

2 Method

We introduce the proposed approach in a general setting first, and then specify its concrete application to separating respiratory and cardiac motion in dynamic MR images.

Consider a linear, discretized dynamic imaging inverse problem with data $(y_t)_{t=1}^T \subset \mathbb{R}^M$ and linear operators $A_t \in \mathcal{L}(\mathbb{R}^{N_1 \times N_2}, \mathbb{R}^M)$ of the form

$$y_t = A_t x_t, \quad t = 1, \dots, T, \quad (1)$$

where the unknown is a sequence of images $(x_t)_{t=1}^T$ with $x_t \in \mathbb{R}^{N_1 \times N_2}$ for each t . Following the basic idea introduced in [25] for static images, we consider each frame $x_t \in \mathbb{R}^{N_1 \times N_2}$ to be the output of a generator $x_t = G_\theta(z_t)$, whose parameters we want to learn only from the given data. In particular, we consider generator networks $G_\theta : \mathbb{R}^q \rightarrow \mathbb{R}^{N_1 \times N_2}$ of the form

$$G_\theta(z_t) = \theta_L^1 * \sigma_{L-1}(\theta_{L-1}^1 * (\dots \sigma_1(\theta_1^1 * z_t + \theta_1^2) \dots) + \theta_{L-1}^2) + \theta_L^2, \quad (2)$$

with time-independent parameters $\theta_j^i \in \Theta$, for $1 \leq i \leq 2$ and $1 \leq j \leq L$ and pointwise nonlinearities $\sigma_1, \dots, \sigma_{L-1}$. The generator network maps the latent space \mathbb{R}^q to the image (frame) space $\mathbb{R}^{N_1 \times N_2}$. Assuming the dynamic image sequence $(x_t)_{t=1}^T$ contains $m \in \{2, 3, \dots\}$ independent types of motion, we split the latent variable $z \in \mathbb{R}^q$ into a time-independent part $z^0 \in \mathbb{R}^{q-m}$ and m time-dependent variables $(z_t^i)_{t=1}^T$ with $z_t^i \in \mathbb{R}$, $i = 1, \dots, m$. We further assume that all the time dependent variables $(z_t^i)_{t=1}^T$ except $(z_t^1)_{t=1}^T$ are given as $(\hat{z}_t^i)_{t=1}^T$ from some one-dimensional a-priori information on the state of the respective types of motion (e.g. from electrocardiograms or accelerometer data).

We then reconstruct the image sequence $(x_t)_{t=1}^T$ together with the network parameters θ , the static latent variable $z^0 \in \mathbb{R}^{q-m}$ and the time-dependent variable $(z_t^1)_{t=1}^T$ via solving

$$(\hat{z}^0, (\hat{z}_t^1)_{t=1}^T, \hat{\theta}) \in \arg \min_{z^0, (z_t^1)_{t=1}^T, \theta} \frac{1}{T} \sum_{t=1}^T \|y_t - A_t G_\theta(z^0, z_t^1, \hat{z}_t^2, \dots, \hat{z}_t^m)\|_2^2, \quad (3)$$

where $\|\cdot\|_2$ is the Euclidean norm (but can be a more general loss). Once a solution is obtained, we do not only obtain the reconstructed images sequence $(\hat{x}_t)_{t=1}^T$ via $\hat{x}_t = G_{\hat{\theta}}(\hat{z}^0, \hat{z}_t^1, \dots, \hat{z}_t^m)$, but, more importantly, can generate image sequences $(\hat{x}_t^i)_{t=1}^T$ for $i = 1, \dots, m$, which we expect to contain only the i th type of motion with all others being fixed, via

$$\hat{x}_t^i = G_{\hat{\theta}}(\hat{z}^0, \hat{z}_{h_1}^1, \dots, \hat{z}_{h_{i-1}}^{i-1}, \hat{z}_t^i, \hat{z}_{h_{i+1}}^{i+1}, \dots, \hat{z}_{h_m}^m), \quad (4)$$

where $h_1, \dots, h_{i-1}, h_{i+1}, \dots, h_m$ are fixed reference frames.

As a concrete example, in this paper we consider the application of this general approach to separating respiratory and cardiac motion in dynamic MR images, where one-dimensional information about the respiratory state (e.g. from an accelerometer) is available. In this case, $m = 2$, and the latent variable $z_t \in \mathbb{R}^q$ at time t is decomposed as $z_t = (z^0, z_t^1, z_t^2)$ with z_t^2 known (and given as $(\hat{z}_t^2)_{t=1}^T$). As our focus is on motion separation rather than reconstruction, we further assume the dynamic image sequence to be available, i.e., A_t is the identity, noting that a generalization of our approach

to reconstruction does not pose any conceptual difficulties. In summary, this yields the following optimization problem

$$(\hat{z}^0, (\hat{z}_t^1)_{t=1}^T, \hat{\theta}) \in \arg \min_{z^0, (z_t^1)_{t=1}^T, \theta} \frac{1}{T} \sum_{t=1}^T \|y_t - G_\theta(z^0, z_t^1, \hat{z}_t^2)\|_2^2. \quad (5)$$

Algorithmic strategy To solve the minimization problem (5), we use Pytorch [45] and the ADAM optimizer [46] with default settings. To achieve a good minimization of the loss, and in particular stability w.r.t varying random initializations (see also Subsection 3.3 below), we iteratively reduce the learning rate after a fixed number of epochs, track the network parameters and latent variables that achieve the minimal loss, and export those parameters and variables as the optimal solution (instead of the variables of the last iterate). Note that this does not cause much computational overhead due to the rather small dimensionality of our network (see Section 3 for details).

3 Numerical Experiments

In this section the results of several experiments concerning dynamic MRI with respiratory and cardiac motion are presented to illustrate the behavior of the new method. In particular, we present a synthetic phantom example and two semi-synthetic examples where real dynamic cardiac MR images were enriched with synthetic respiratory motion. Results for two additional real dynamic cardiac MR images are provided in the appendix. In addition, the ancillary files for this article contain videos for all results. For all experiments, we assume one-dimensional information about the respiratory motion to be given. For the phantom data, we also experiment with having one-dimensional information about both motion types given and use that as a reference scenario.

To assess the quality of the motion separation, we compute the relative error norms (\mathbf{E}_h^1 and \mathbf{E}_h^2) of the dynamic images $\hat{x}^1 = (\hat{x}_t^1)_{t=1}^T$, $\hat{x}^2 = (\hat{x}_t^2)_{t=1}^T$ containing just one reconstructed kind of movement, where

$$\mathbf{E}_h^1 = \|\hat{x}^1 - x_{\text{true}}^1\|_2 / \|x_{\text{true}}^1\|_2, \quad \mathbf{E}_h^2 = \|\hat{x}^2 - x_{\text{true}}^2\|_2 / \|x_{\text{true}}^2\|_2, \quad (6)$$

and x_{true}^i is the ground truth showing only the i th type of motion, i.e., cardiac motion for $i = 1$ and respiratory motion for $i = 2$. Here, the subscript h refers to the frame at which the other motion state is fixed, see (4).

In principle, as described in Section 2, our method allows to freeze one kind of motion at any state, and generate images containing only the second kind of motion, as long as a sufficient mixing of motions was observed. In practice, the choice of the freezing frame h has an impact on the performance of the single motion reconstruction (though for the phantom at an overall rather low error regime). Figure 3b provides an example for this by plotting the errors \mathbf{E}_h^1 and \mathbf{E}_h^2 as a function of the frame h that is fixed for the other kind of motion. In our experiments, we always show results for fixing the motion state that provides the best performance with respect to the ground truth.

For all experiments shown in the paper, we repeated the experiment 20 times with 20 different seeds, and show the result whose performance w.r.t. the error measure \mathbf{E}_h^1 is closest to the median performance. For a discussion on the stability of our method w.r.t varying seeds see Subsection 3.3. Quantitative error measures for all experiments are provided in Table 1. The ancillary files further contain videos showing the best result that was achieved over the 20 seeds for each experiment. The source code to reproduce all experiments is available at [28]. All our experiments were conducted on a workstation with an AMD Ryzen 7 3800X 8-Core Processor and 32 GB of memory, using a Nvidia RTX 3090 GPU with 24 GB of memory. The largest experiment considered here (solving (5) with real cine MR data) took around 3.8 minutes.

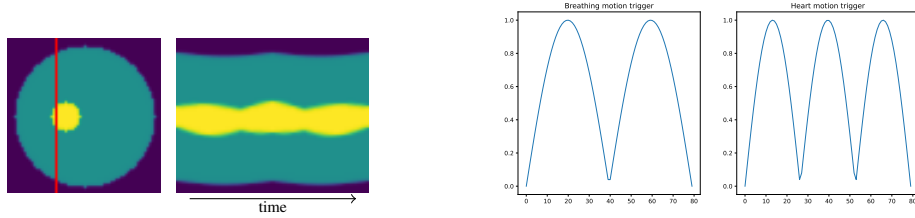
3.1 Synthetic data

The first test problem, consisting of 80 frames with 64×64 pixels, corresponds to a synthetic example displaying two nested disks and is represented in Figure 1. A more compact representation of this dynamic image can be observed in Figure 2a, where a vertical slice of the image (marked in red on the left image), is displayed over time (and can be seen on the right image) clearly showing temporal changes. This representation will be used throughout the paper.

In this example, three cardiac motion cycles are simulated by dilation of the internal disk while two simulated breathing motion cycles are represented by shearing of the whole image. Note that the size of the frames over time is maintained constant. The ground truth one-dimensional motion information, henceforth referred to as motion triggers, that was used to parametrize the different types of motions is displayed in Figure 2b. Note that this is the information that defines one (or both in a reference scenario) of the latent variables $(z^1(t))_{t=1}^T$ and $(z^2(t))_{t=1}^T$.



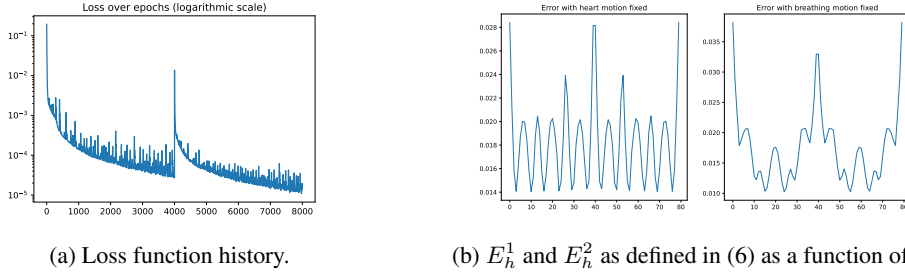
Figure 1: Selected phantom frames displaying different phases of respiratory and cardiac movement.



(a) Compact representation of the video.

(b) Ground truth motion triggers.

Figure 2: Alternative representation of the time evolution for the synthetic data.



(a) Loss function history.

(b) E_h^1 and E_h^2 as defined in (6) as a function of h .

Figure 3: Loss function plot and error w.r.t. fixing different frames for the second phantom experiment.

The generator modeling the solution for this example, as defined in Equation (2), corresponds to a standard deep convolutional neural network (CNN) with 5 layers, where transpose two-dimensional convolutions are used for all convolutions in (2) and no biases are used. The network parameters are given as follows. Number of channels: $[64, 128, 64, 32, 16, 1]$, (square) kernel size: $[4, 4, 4, 4, 4]$, stride: $[1, 2, 2, 2, 2]$, padding: $[0, 1, 1, 1, 1]$, activation functions: $[\text{Tanh}, \text{LeakyReLU}, \text{Tanh}, \text{LeakyReLU}, \text{Tanh}]$. In total, the network has 3.03360×10^5 parameters. The latent space $Z \in \mathbb{R}^{64}$ is split into 62 static components and 2 dynamic components. Blocks of $[4000, 4000]$ epochs with learning rates $[0.01, 0.005]$ are used for the Adam optimizer. An example plot of the loss value history throughout the iterations can be found in Figure 3a. The latent variables are always initialized randomly from a uniform distribution on the interval $[0, 1)$, and the network weights are initialized orthogonally following [47].

The dynamic image reconstruction is performed in two different scenarios. First, as reference scenario, we consider both motion triggers associated to the two types of movements (as displayed in Figure 2b) to be known. In this case, we use them as the temporal-dependent latent variables $(z_t^1)_{t=1}^T$ and $(z_t^2)_{t=1}^T$. We optimize the network over the network weights θ and the static component z^0 .

Second, we assume that one of the dynamic components in the latent space, $(z_t^1)_{t=1}^T$ corresponding to the cardiac motion, is unknown. We then use the framework defined in Equation (5), and we optimize the network over the network weights θ and the components of the latent space $(z_t^1)_{t=1}^T$ and z^0 .

The reconstruction of the dynamic image in both cases is shown in Figure 4. Even though a representation of the given data with mixed motion is not our primary goal, it can still be observed that both representations are visually very similar to the ground truth, giving evidence that one-dimensional information on one of the movements is enough to disentangle the latent space without a significant degradation in representing the data.

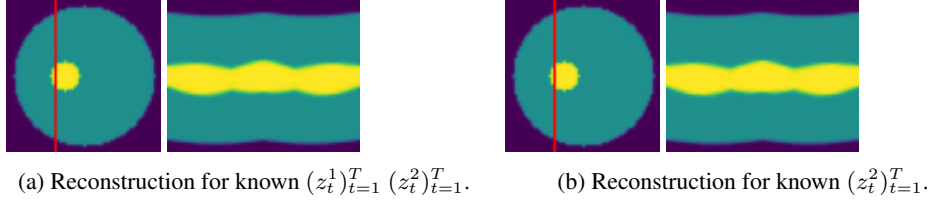


Figure 4: Synthetic video reconstruction with full motion.

Using the strategy described in Section 2, motion separation is performed in the case where both motion triggers, $(z_t^1)_{t=1}^T$ and $(z_t^2)_{t=1}^T$, are known, and in the case where just $(z_t^2)_{t=1}^T$ is known. Figure 5 shows the isolated cardiac motion reconstructions, while Figure 6 shows the isolated respiratory motion reconstructions. Similarly to Figure 4, it can also be observed that single-motion reconstructions for either one or two known triggers are visually very close to the ground truth. This is especially meaningful for the reconstruction of cardiac motion in Figure 5d, where no prior information on the motion is used, supporting our hypothesis that latent space disentanglement is a meaningful tool for motion separation and reconstruction.

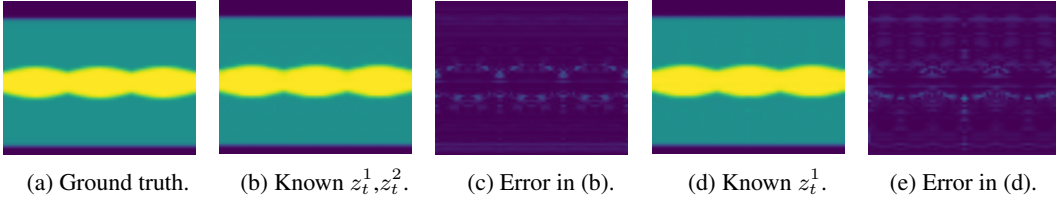


Figure 5: Compact representation of the synthetic video reconstructions with only cardiac motion. Error images are upscaled by a factor of 10.

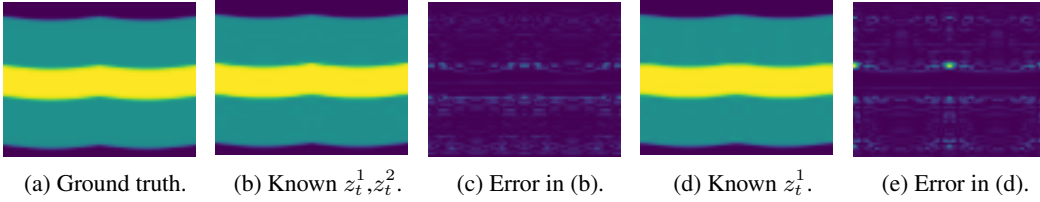


Figure 6: Compact representation of the synthetic video reconstructions with only respiratory motion. Error images are upscaled by a factor of 10.

3.2 Real MRI data

After exploring the potential of the method on synthetic data, we test it in real cine MRI datasets, comprising datasets with a four-chamber view and datasets with a short-axis view. We provide results for two datasets in this section, and results for two additional datasets in the appendix. Table 1 provides error measures for all experiments. All real data used in this work comes from the datasets that were made available by the organizers of the ISMRM reconstruction challenge 2014¹. In all real datasets, the original videos were obtained via a sum-of-squares reconstruction from fully sampled MR data, and contain a 2D slice of the entire thorax showing the beating heart in one region. For our experiments, we simulated three heartbeats by concatenating the single-heartbeat-videos three times, and simulated two respiratory cycles with vertical (resp. horizontal) shearing motion for the

¹challenge.ismr.org. Permission to use the data in research was obtained from the organizers per mail.

four-chamber (resp. short-axis) view. After obtaining videos showing a slice of the entire thorax with three heartbeats and two breaths, we cropped the videos to a region of interest around the heart, see the top rows of Figures 13 and 15 for the original data that is used as the input to our method. The final data consists of 99 frames with spatial resolution 100×100 for the four-chamber view, and of 81 frames with spatial resolution 70×70 for the short-axis view.

In all experiments with real data, the generator is a standard deep convolutional neural network (CNN) with 7 layers, ReLU activation functions in the first and last layer, LeakyReLUs in the middle layers and no biases. The latent space \mathbb{R}^{100} is split into 98 static components and 2 dynamic components. Network parameters shared by all experiments are given as: Number of channels: [100, 640, 320, 160, 80, 40, 20, 1], stride: [2, 2, 2, 2, 2, 2, 1]. To account for the different image dimensions, the shape of the remaining parameters differs slightly: (Square) kernel size: [4, 4, 4, 4, 4, 4, 3] (four-chamber), [4, 4, 4, 4, 4, 5, 4] (short-axis), padding: [0, 2, 0, 2, 2, 1, 1] (four-chamber), [0, 2, 2, 2, 2, 1, 1] (short-axis). In total, the networks have 5.388980×10^6 (four-chamber) and 5.396320×10^6 (short-axis) parameters.

The network is optimized according to Equation (5), where z^0 and $(z_t^1)_{t=1}^T$ are randomly initialized from a uniform distribution on the interval $[0, 1]$, and the network weights are initialized according to the Pytorch self-initialization. For both experiments, blocks of [4000, 4000, 4000, 4000, 4000] epochs with learning rates [0.01, 0.008, 0.005, 0.003, 0.001] are used for the Adam optimizer.

Motion separation and correction is performed on the real MRI data as explained in Section 2. The learned generator and the reconstructed dynamic latent space variables are then used to freeze one type of motion while maintaining the dynamics of the other type of motion. The latent space variables associated to the cardiac motion are shown in Figures 7a and 7b for the four-chamber and short-axis view, respectively. Note that these plots have a physical interpretation associated to the heart’s activity, and were completely unknown before performing the optimization.

The results of the motion separation experiments are shown in Figures 8 and 9 for the four-chamber view experiment and in Figures 10 and 11 for the short-axis view experiment. In Figures 8 and 10, the top row shows selected frames of the given image sequence, containing both cardiac and respiratory motion. The bottom row shows a generated image sequence with only cardiac motion. Figures 9 and 11 show a reference frame with a marked slice (first column), the dynamics of the slice over time for the ground truth (second and fifth column) and for the generated image sequence (third and sixth column), and a difference image (third and seventh column). Columns two to four show the isolated cardiac motion, columns five to seven show the isolated breathing motion.

It can be observed that in both cases and for both types of motion, the separation of motion works well, and the different structures of the motion are clearly visible in the slice-based visualization of the generated images. This is also confirmed by the quantitative values provided in Table 1. We should note that some artifacts are visible in the breathing motion reconstruction. In our experience, those are mostly related to having obtained a sub-optimal solution of the minimization problem (recall that we provide results corresponding to the median of the performance of our method). In cases where a favorable random initialization leads to an improved convergence of the methods these artifacts are reduced, see for instance the videos showing the best result that was achieved over the 20 seeds as provided in the ancillary files.

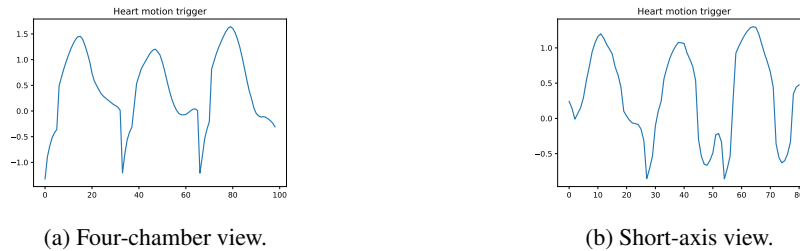


Figure 7: Motion triggers for the two real MRI reconstructed videos with only cardiac motion.

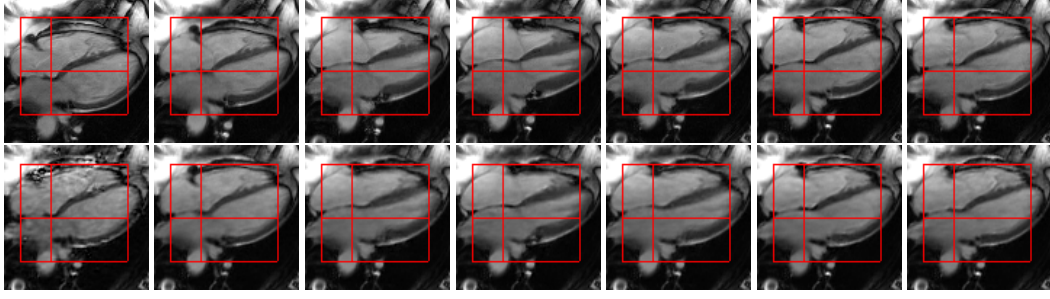


Figure 8: Four-chamber view. First row: Representative frames of the original video. Second row: Reconstructed video with only cardiac motion.

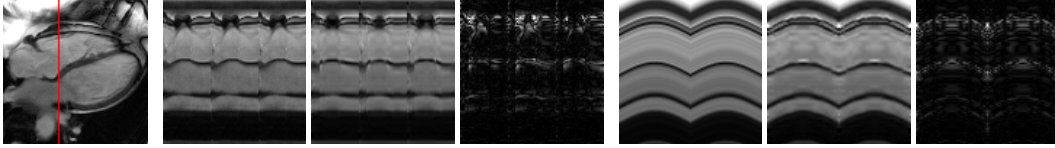


Figure 9: Four-chamber view. First image: Reference frame with marked slice, second (resp. fifth) image: slice over time for ground truth with only cardiac (resp. respiratory) motion, third (resp. sixth) image: slice over time for reconstructed images with only cardiac (resp. respiratory) motion, fourth and seventh image: difference between ground truth and reconstructed (upscaled by a factor of two).



Figure 10: Short-axis view. First row: Representative frames of the original video. Second row: Reconstructed video with only cardiac motion.

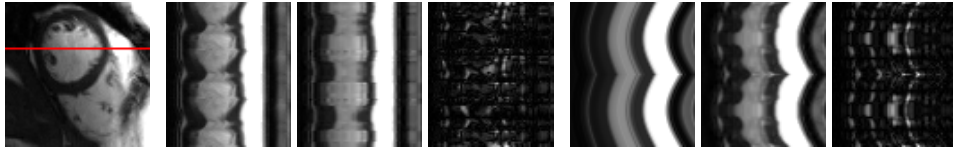


Figure 11: Short-axis view. First image: Reference frame with marked slice, second (resp. fifth) image: slice over time for ground truth with only cardiac (resp. respiratory) motion, third (resp. sixth) image: slice over time for reconstructed images with only cardiac (resp. respiratory) motion, fourth and seventh image: difference between ground truth and reconstructed (upscaled by a factor of two).

3.3 Stability with respect to initialization

To study the stability of the method with respect to the initialization of the parameters, the reconstruction and motion separation are repeated for 20 different seeds for each of the experiments in this paper, see Table 1 for an evaluation. It can be observed that the method is rather stable on average, with few (in practice 1-2 per 20 seeds) negative outliers. In our experiments, negative outliers were always connected to the loss of the final result still being comparatively high. Consequently, in application, these outliers can be detected by a high value of the loss (without knowing the ground truth), and the method can be re-run with a different initialization in such cases.

Table 1: Error in separation of different kinds of motion for the experiments considered in this paper, repeating them for 20 different seeds. MAD denotes the median absolute deviation.

	Median	MAD	Mean	Std. dev.
Phantom example, z^1, z^2 known - \mathbf{E}_h^1 (cardiac)	4.86e-03	2.40e-04	4.89e-03	4.58e-04
Phantom example, z^1, z^2 known - \mathbf{E}_h^2 (resp.)	6.65e-03	3.83e-04	6.51e-03	8.81e-04
Phantom example, z^2 known - \mathbf{E}_h^1 (cardiac)	9.93e-03	1.05e-03	1.03e-02	1.97e-03
Phantom example, z^2 known - \mathbf{E}_h^2 (respiratory)	1.20e-02	1.09e-03	1.22e-02	1.39e-03
Four-chamber view - \mathbf{E}_h^1 (cardiac)	1.01e-01	2.25e-02	1.21e-01	4.84e-02
Four-chamber view - \mathbf{E}_h^2 (respiratory)	8.29e-02	1.94e-02	9.34e-02	3.88e-02
Short-axis view - \mathbf{E}_h^1 (cardiac)	8.07e-02	1.21e-02	9.21e-02	2.83e-02
Short-axis view - \mathbf{E}_h^2 (respiratory)	7.21e-02	1.41e-02	8.29e-02	3.20e-02
Four-chamber view, example 2 - \mathbf{E}_h^1 (cardiac)	9.02e-02	7.55e-03	1.07e-01	4.84e-02
Four-chamber view, example 2 - \mathbf{E}_h^2 (resp.)	7.52e-02	1.14e-02	9.24e-02	5.90e-02
Short-axis view, example 2 - \mathbf{E}_h^1 (cardiac)	1.36e-01	3.41e-02	1.42e-01	3.84e-02
Short-axis view, example 2 - \mathbf{E}_h^2 (respiratory)	1.05e-01	2.50e-02	1.14e-01	3.27e-02

Conclusions and outlook

This paper presents a new method for motion separation based on the joint optimization of an untrained generator network over both the network parameters and the latent codes. Assuming one-dimensional information on all but one of the motions is known, motion separation is achieved through latent space disentanglement. Feasibility of this method was shown for separating respiratory and cardiac motion in dynamic MRI, but the proposed method is general and can conceptually be used in many applications, e.g., in bio-medical imaging, bio-mechanics or physics.

A limitation of the method, resulting from non-convexity of the underlying minimization problem, is its dependence on initializations. While in the examples considered in this paper, robustness w.r.t. initializations was achieved via restarting strategies paired with appropriately decaying learning rates, more advanced solution strategies will be necessary to achieve an out-of-the-box applicability of the method in different application scenarios, in particular when the given image data is observed only indirectly via a measurement operator.

Our work shows a great potential of latent space disentanglement on untrained generators for video data. It opens the door to more advanced disentanglement schemes (e.g., based on modifications of the loss function or additional constraints on the latent space variables). Moreover, we expect the proposed method to be very well suited as image prior for dynamic inverse problems (e.g., in tomography, super-resolution) where the reconstructed solution displays different kinds of independent motion.

References

- [1] M L Wood, R M Henkelman, MR image artifacts from periodic motion, Medical Physics, 1985;12(2):143-51.
- [2] R V D Walle, I Lemahieu, E Achten, Magnetic resonance imaging and the reduction of motion artifacts: Review of the principles. Technol Health Care, 1997;5(6):419-435.
- [3] D L Bihan, C Poupon, A Amadon, F Lethimonnier, Artifacts and pitfalls in diffusion MRI. Journal of Magnetic Resonance Imaging, 2006;24(3):478-488.

- [4] T Beyer et al. Dual-modality PET/CT imaging: the effect of respiratory motion on combined image quality in clinical oncology, *European Journal of Nuclear Medicine and Molecular Imaging*, 2003;30(4):588-596.
- [5] M M Osman, C Cohade, Y Nakamoto, R L Wahl, Respiratory motion artifacts on PET emission images obtained using CT attenuation correction on PET-CT, *European Journal of Nuclear Medicine and Molecular Imaging*, 2003;30(4):603-606.
- [6] C R R N Hunter, R Klein, R S Beanlands, R A deKemp, Patient motion effects on the quantification of regional myocardial blood flow with dynamic PET imaging, *Medical Physics*, (2016);43(4):1829.
- [7] C Liu, L A Pierce, A M Alessio, P E Kinahan, The impact of respiratory motion on tumor quantification and delineation in static PET/CT imaging, *Physics in Medicine and Biology*, 2009;54(24):7345-7362.
- [8] V Bettinardi et al. Detection and compensation of organ/lesion motion using 4D-PET/CT respiratory gated acquisition techniques, *journal of the European Society for Therapeutic Radiology and Oncology*, 2010;96(3):311-316.
- [9] J R McClelland, D J Hawkes, T Schaeffter, A P King, Respiratory motion models: A review, *Medical Image Analysis*, 2013;17(1):19-42.
- [10] V Bettinardi, E D Bernardi, L Presotto, M C Gilardi, Motion-Tracking Hardware and Advanced Applications in PET and PET/CT, *PET Clinics*, 2013;8(1):11-28.
- [11] D Visvikis F, Lamare, P Bruyant, N Bousson, C C L Rest, Respiratory motion in positron emission tomography for oncology applications: Problems and solutions, *Nuclear Instruments and Methods in Physics Research Section A: Accelerators, Spectrometers, Detectors and Associated Equipment*, 2006;569(2):453-457.
- [12] S A Nehmeh, Y E Erdi, Respiratory motion in positron emission tomography/computed tomography: a review, *Seminars in Nuclear Medicine*, 2008;38(3):167-176.
- [13] F Lamare et al. PET respiratory motion correction: Quo vadis?, *Physics in Medicine and Biology*, 2022;67(3).
- [14] M Zaitsev, J Maclaren, M Herbst, Motion Artifacts in MRI: A Complex Problem With Many Partial Solutions, *Journal of Magnetic Resonance Imaging*, 2015;42:887-901.
- [15] A Rahmim, O Rousset, H Zaidi, Strategies for Motion Tracking and Correction in PET, *PET clinics*, 2007;2(2):251-266.
- [16] A Gillman, J Smith, P Thomas, S Rose, N Dowson, PET motion correction in context of integrated PET/MR: Current techniques, limitations, and future projections, *Medical Physics*, 2017;44(12):430-445.
- [17] J V D Hoff, J Maus, G Schramm, Motion compensation in emission tomography, *Handbook of Particle Detection and Imaging*, Springer International Publishing, 2020;1-47.
- [18] A Z Kyme, R R Fulton, Motion estimation and correction in SPECT, PET and CT, *Physics in Medicine and Biology*, 2021;15;66(18).
- [19] I Polycarpou, G Soultanidis, C, Tsoumpas, Synergistic motion compensation strategies for positron emission tomography when acquired simultaneously with magnetic resonance imaging, *Philosophical Transactions of the Royal Society A*, 2021;379(2204).
- [20] G J Klein, B W Reutter, E H Botvinick, T F Budinger, R H Huesman, Fine-scale motion detection using intrinsic list mode PET information, *Workshop on Mathematical Methods in Biomedical Image Analysis*, IEEE Computer Society, Los Alamitos, CA, USA, 2001;71-78.
- [21] R A Bundschuh et al. Postacquisition detection of tumor motion in the lung and upper abdomen using list-mode PET data: a feasibility study, *Journal of nuclear medicine : official publication, Society of Nuclear Medicine*, 2007;48(5):758-763.
- [22] F Büther et al. List mode-driven cardiac and respiratory gating in PET, *Journal of Nuclear Medicine*, 2009;50(5):674-681.
- [23] J Frahm et al. On the temporal fidelity of nonlinear inverse reconstructions for real time MRI-the Motion Challenge, *The Open Medical Imaging Journal*, 2014;8(1):1-5.
- [24] J Y Cheng et al. Free-breathing pediatric MRI with nonrigid motion correction and acceleration, *Journal of Magnetic Resonance Imaging*, 2015;42(2):407-20.

- [25] D Ulyanov, A Vedaldi, V Lempitsky, Deep image prior, *International Journal of Computer Vision*, 2020;128:1867-1888.
- [26] H C Burger, C J Schuler, S Harmeling, Image denoising: Can plain neural networks compete with BM3D? 2012 IEEE Conference on Computer Vision and Pattern Recognition, 2012;2392-2399.
- [27] A Habring, M Holler, A Generative Variational Model for Inverse Problems in Imaging, *SIAM Journal on Mathematics of Data Science*, 2022;4(1): 306-335.
- [28] Abdullah, M Holler, K. Kunisch, M. S. Landman. Source code for the paper *Nonlinear motion separation via untrained generator networks with disentangled latent space variables and applications to cardiac MRI*. github.com/holler/m/generator_based_motion_separation. 2022.
- [29] E Kang, W Chang, J Yoo, J C Ye, Deep convolutional framelet denosing for low-dose CT via wavelet residual network," *IEEE Transactions on Medical Imaging*, 2018;37(6):1358-1369.
- [30] J Yoo et al. Deep learning diffuse optical tomography," *IEEE Transactions on Medical Imaging*, 2019; 39(4):877-887.
- [31] K H Jin, M T McCann, E Froustey, M Unser, Deep convolutional neural network for inverse problems in imaging," *IEEE Transactions on Image Processing*, 2017;26(9):4509-4522.
- [32] Y Yang, J Sun, H Li, Z Xu, Deep ADMM-Net for compressive sensing MRI, *Advances in Neural Information Processing Systems*, 2016;10-18.
- [33] K Hammernik et al. Learning a variational network for reconstruction of accelerated MRI data, *Magnetic Resonance in Medicine*, 2018;79(6):3055-3071.
- [34] K C Tezcan et al. MR image reconstruction using deep density priors, *IEEE Transactions on Medical Imaging*, 2019;38(7):1633-1642.
- [35] M Mardani et al. Deep generative adversarial neural networks for compressive sensing MRI, *IEEE Transactions on Medical Imaging*, 2019;38(1):167-179.
- [36] K Gong, C Catana, J Qi, Q Li, PET Image Reconstruction Using Deep Image Prior, *IEEE Transactions on Medical Imaging*, 2019;38(7):1655-1665.
- [37] R Hyder, M S Asif, Generative models for low-rank video representation and reconstruction from compressive measurements, *IEEE 29th International Workshop on Machine Learning for Signal Processing (MLSP)*, 2019:1-6
- [38] J Yoo et al. Time-dependent deep image prior for dynamic MRI, *IEEE Transactions on Medical Imaging*, 2021;40(12):3337-3348.
- [39] C Vondrick, H Pirsiavash, A Torralba, Generating Videos with Scene Dynamics, *Advances in Neural Information Processing Systems*, 2016:613-621.
- [40] M Saito, E Matsumoto, S Saito, Temporal Generative Adversarial Nets with Singular Value Clipping, *IEEE International Conference on Computer Vision (ICCV)*, 2017:2849-2858.
- [41] S Tulyakov, M Y Liu, X Yang, J Kautz, "MoCoGAN: Decomposing Motion and Content for Video Generation, *IEEE Conference on Computer Vision and Pattern Recognition (CVPR)*, 2018;1526-1535.
- [42] X Chen et al. InfoGAN: Interpretable representation learning by information maximizing generative adversarial nets, *Advances in Neural Information Processing Systems*, 2016:2180-2188.
- [43] K Liu, Towards Disentangling Latent Space for Unsupervised Semantic Face Editing, 2021, *arXiv preprint arXiv:2011.02638*.
- [44] P Bojanowski, A Joulin, D L Paz, A Szlam, Optimizing the Latent Space of Generative Networks, *Proceedings of the 35 th International Conference on Machine Learning*, 2018.
- [45] A Paszke et al. Automatic differentiation in PyTorch, *Advances in Neural information processing systems*, 2017.
- [46] D P Kingma, B Jimmy, Adam: A method for stochastic optimization, 2014, *arXiv preprint arXiv:1412.6980*.
- [47] A Saxe, J L McClelland, S Ganguli, Exact solutions to the nonlinear dynamics of learning in deep linear neural network, *International Conference on Learning Representations*, 2014.

A Appendix

In this appendix, we present results as shown in the paper for two more real MRI data experiments, one with a four-chamber view (Figures 13 and 14) and one with a short-axis view (Figures 15 and 16). The estimated latent space variables associated to the cardiac motion are shown in Figure 12.

It can be observed that, again, in both cases the separation of cardiac and respiratory motion works well with the proposed method. In particular for the short-axis view, as can be seen in Figure 16, the separation of respiratory motion is even better than with the short-axis example shown in the paper. In this case, however, the reconstructed motion trigger for the cardiac motion is inaccurately reconstructed for the second heartbeat. Again, note that we present result corresponding to the median performance of the methods over repeating each experiment 20 times with 20 different seeds for the random initialization. In case of a favorable random initialization, convergence of the method and, consequently, also the corresponding results are improved, see for instance the videos provided in the ancillary files.

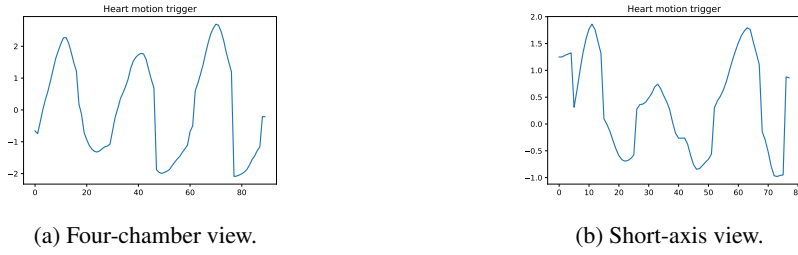


Figure 12: Motion triggers for the two real MRI reconstructed videos with only cardiac motion.

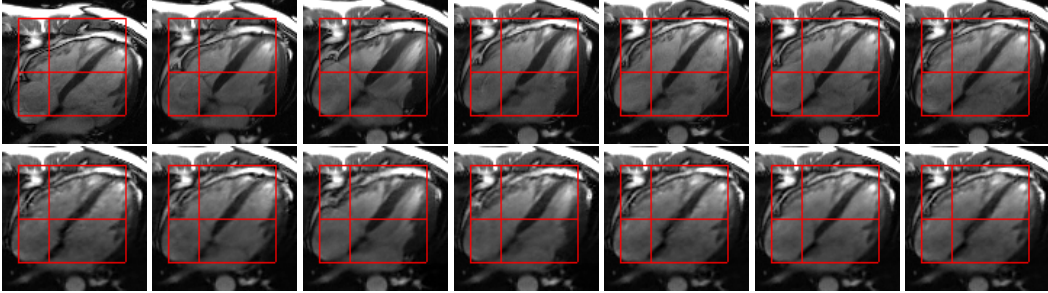


Figure 13: Four-chamber view. First row: Representative frames of the original video. Second row: Reconstructed video with only cardiac motion.

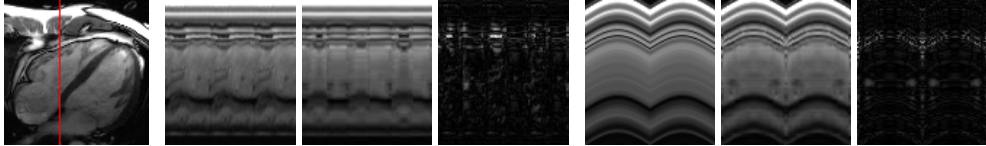


Figure 14: Four-chamber view. First image: Reference frame with marked slice, second (resp. fifth) image: slice over time for ground truth with only cardiac (resp. respiratory) motion, third (resp. sixth) image: slice over time for reconstructed images with only cardiac (resp. respiratory) motion, fourth and seventh image: difference between ground truth and reconstructed (upscaled by a factor of two).

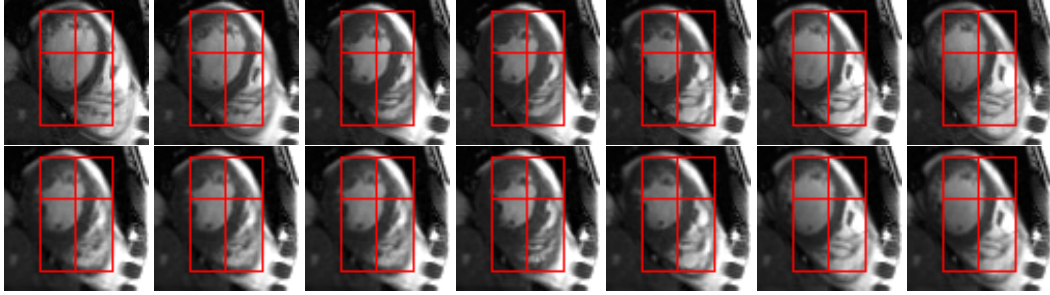


Figure 15: Short-axis view. First row: Representative frames of the original video. Second row: Reconstructed video with only cardiac motion.

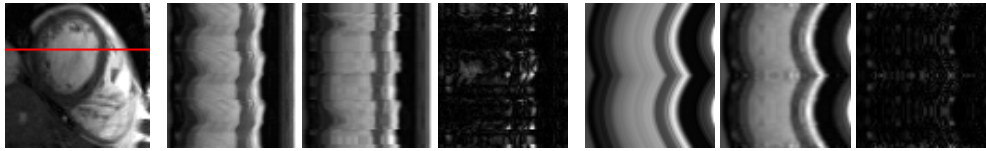


Figure 16: Short-axis view. First image: Reference frame with marked slice, second (resp. fifth) image: slice over time for ground truth with only cardiac (resp. respiratory) motion, third (resp. sixth) image: slice over time for reconstructed images with only cardiac (resp. respiratory) motion, fourth and seventh image: difference between ground truth and reconstructed (upscaled by a factor of two).